



Article

Tuning Molten-Salt-Mediated Calcination in Promoting Single-Crystal Synthesis of Ni-Rich $\text{LiNi}_x\text{Mn}_y\text{Co}_z\text{O}_2$ Cathode Materials

Joon Kyung Koong and George P. Demopoulos *

Department of Materials Engineering, McGill University, Montreal, QC H3A 0G4, Canada;
joon.koong@mail.mcgill.ca

* Correspondence: george.demopoulos@mcgill.ca

Abstract: High Ni-content $\text{LiNi}_x\text{Mn}_y\text{Co}_z\text{O}_2$ (NMC) cathodes (with $x \geq 0.8$, $x + y + z = 1$) have gained attention recently for their high energy density in electric vehicle (EV) Li-ion batteries. However, Ni-rich cathodes pose challenges in capacity retention due to inherent structural and surface redox instabilities. One promising strategy is to make the Ni-rich NMC material in the form of single-crystal micron-sized particles, as they resist intergranular and surface degradation during cycling. Among various methods to synthesize single-crystal NMC (SC-NMC) particles, molten-salt-assisted calcination offers distinct processing advantages but at present, is not yet optimized or mechanistically clarified to yield the desired control over crystal growth and morphology. In this project, molten-salt-mediated transformation of $\text{Ni}_{0.85}\text{Mn}_{0.05}\text{Co}_{0.15}(\text{OH})_2$ precursor (P-NMC) particles to $\text{LiNi}_{0.85}\text{Mn}_{0.05}\text{Co}_{0.15}\text{O}_2$ particles is investigated in terms of the crystal growth mechanism and its electrochemical response. Unlike previous studies that involved large volumes of molten salt, using a smaller volume of molten KCl is found to result in larger primary particles with improved cycling performance achieved via partial reactive dissolution and heterogeneous nucleation growth, suggesting that the ratio of molten salt volume to NMC mass is an important parameter in the synthesis of single-crystal Ni-rich NMC materials.



Citation: Koong, J.K.; Demopoulos, G.P. Tuning Molten-Salt-Mediated Calcination in Promoting Single-Crystal Synthesis of Ni-Rich $\text{LiNi}_x\text{Mn}_y\text{Co}_z\text{O}_2$ Cathode Materials. *Batteries* **2024**, *10*, 387. <https://doi.org/10.3390/batteries10110387>

Academic Editor: Claudio Gerbaldi

Received: 23 September 2024

Revised: 18 October 2024

Accepted: 30 October 2024

Published: 2 November 2024



Copyright: © 2024 by the authors. Licensee MDPI, Basel, Switzerland. This article is an open access article distributed under the terms and conditions of the Creative Commons Attribution (CC BY) license (<https://creativecommons.org/licenses/by/4.0/>).

1. Introduction

Li-ion batteries (LIBs) have become an indispensable part of modern society, from powering portable devices to grid-scale energy storage systems. Recently, their role has expanded into electric vehicles (EVs) as their energy storage system, resulting in an ever-growing demand for improvements in energy density and longevity [1–3]. In particular, the cathode is at the center of battery research, as it is not only the key determinant of battery cost but is also currently the limiting factor in LIB performance [4–6].

Among various cathode materials, $\text{LiNi}_x\text{Mn}_y\text{Co}_z\text{O}_2$ (NMC) has been gaining significant attention for its high energy density, with a noticeable shift towards nickel-rich compositions ($x \geq 0.8$) to reduce cobalt dependency and increase energy density [7,8]. However, Ni-rich NMC suffers from structural and interfacial instability, causing degradation of the electrode and significantly affecting the overall electrochemical performance [9,10]. The polycrystalline structure of NMC exacerbates these degradations due to its weak grain boundaries, which are prone to cracking, exposing new surfaces for parasitic side reactions with the electrolyte [11–15].

To alleviate the structural instability of polycrystalline NMC (PC-NMC), there has been a shift towards single-crystal NMC (SC-NMC) that has shown improved stability and cycle life owing to its boundary-free grains and consistent lattice parameters [16–20]. Among the various synthesis methods for SC-NMC, molten-salt-assisted calcination has

been recognized to offer promising potentials for controlling particle size, morphology, and faceting. Nonetheless, a comprehensive and in-depth understanding of the crystallization mechanism is still required to fully optimize the molten-salt-assisted calcination process and achieve the desired control over particle characteristics.

Typically, in molten-salt-assisted calcination, precursor particles, such as $\text{Ni}_{0.8}\text{Mn}_{0.1}\text{Co}_{0.1}(\text{OH})_2$ (P-NMC), are mixed with a lithium source and a low-melting-point salt, heated in an oxygen-rich atmosphere. The molten salt facilitates dissolution and recrystallization of NMC particles, promoting grain growth through mass transport and Ostwald ripening, ultimately resulting in well-grown single crystals [21]. Because molten-salt-assisted calcination allows us to obtain high crystallinity SC-NMC at a relatively low calcination temperature, many studies have been conducted to research the effect of it on the cathode's performance. Kim et al. synthesized SC-NMC using alkali chlorides as the molten salt and demonstrated that the choice of salt affects particle morphology, with KCl yielding round-like particles and vague facets, while NaCl produces octahedral-shaped particles with clear facets [22]. Despite the advantage of molten-salt-assisted calcination in obtaining well-defined faceted SC-NMCs, these particles often have lower volumetric energy density, an important performance metric for batteries. Moiseev et al. addressed this by tuning the particle morphology into a spherical shape using different ratios of lithium sources in a K_2SO_4 flux, thereby improving the tap density and volumetric energy density [23]. Spence et al. studied the effect of a double salt flux composition and discovered that varying the LiCl to KCl ratio affects the crystal morphology and its working calcination temperature, underscoring the need for further studies in optimizing the molten salt composition for optimal performance of the cathode [24]. Mixing different types of salt and their ratio to obtain a eutectic mixture is an effective way to control the temperature at which the mixture reaches a molten state, which can be used as a parameter when synthesizing SC-NMC. Although not directly applied to SC-NMC synthesis, Qin used the eutectic point of a LiOH-NaCl system, where a specific molar ratio allowed the mixture to reach a molten state at relatively low temperatures, driving the relithiation reaction and phase reconstruction in spent NMC [20].

Most studies on molten-salt-based synthesis utilize a large volume of molten salt to ensure effective dissolution and recrystallization of NMC particles, typically with a salt-to-precursor molar ratio between 4 and 30 [22–24]. However, using large molten salt volumes is impractical for scale-up due to increased costs, higher chemical waste generation, and the need for excessive washing steps, which may adversely affect the cathode's electrochemical performance, as this leads to inferior air stability [25]. Qu et al. synthesized NMC532 using lower salt amounts, from 5% to 110% excess Li/TM, with Li_2CO_3 acting both as a lithium source and molten salt, finding that increased excess lithium content initially increased the primary particle size and improved the cycle life [26]. However, using Li_2CO_3 complicates isolating the effects of lithium from those of the molten salt content on the cathode's electrochemical performance.

Molten-salt-assisted calcination clearly offers substantial control over particle crystal growth, providing opportunities to improve the cycling performance of Ni-rich NMC cathodes. Previous studies have explored the effect of various lithium sources, molten salt types, and ratio of molten salt mixture on NMC crystal morphology and size, providing insights into how molten salt can be utilized in calcination to improve the electrochemical performance of the cathode [20,22–24]. However, conventionally studied large volumes of molten salt baths require an extensive washing step that not only generates significant chemical waste but also raises the manufacturing cost [27]. Therefore, this project focuses on the impact of a reduced molten salt volume during calcination on the crystal size, morphology, and cycling performance of Ni-rich NMC. Furthermore, we aim to unveil the crystallization mechanism and how the molten salt volume influences it, seeking to optimize the molten-salt-assisted calcination process in the synthesis of single-crystal Ni-rich NMC materials.

2. Materials and Methods

2.1. Material Synthesis

A commercial NMC hydroxide precursor (nickel manganese cobalt oxide, NCM811 Cathode Precursor, SKU: LB015-2, LANDT) was used to experiment with different molten-salt-assisted calcination conditions. A full characterization of the precursor is provided in the Supplementary Materials. For the preparation of calcination, the hydroxide precursor (P-NMC) and lithium hydroxide (98% LiOH·H₂O, Sigma-Aldrich, St. Louis, MO, USA), with a molar ratio of Li/TM = 1.05 (TM = transition metal ions, Li = lithium-ion), and various amounts of potassium chloride (99.0–100%, KCl, Sigma-Aldrich) were homogeneously mixed using a mortar and pestle. The Li/TM = 1.05 molar ratio is a commonly chosen value for NMC811 (LiNi_{0.8}Mn_{0.1}Co_{0.1}O₂) synthesis to compensate for the loss of lithium at high-temperature calcination. The mixture was then transferred into a crucible and placed in a tube furnace (OTF-1200X, MTI Corporation, Richmond, CA, USA). The calcination temperature for Ni-rich NMC typically ranges from 800 °C to 950 °C, with durations of 10 to 12 h [28]. Since higher temperatures and prolonged durations can lead to structural defects, the calcination temperature was chosen to be 850 °C for 10 h, with a heating rate of 10 °C/min and cooling rate of 2 °C/min down to 25 °C, to achieve a well-layered structure NMC yet minimize such structural defects. After cooling, the crucible was removed, and the synthesized NMC was thoroughly rinsed with deionized water (DI water) three times using a vortex mixer. The NMC calcined with KCl underwent an additional rinsing step, where it was sonicated for 5 min in DI water to ensure there was no KCl residual. The synthesized NMC was separated from the wastewater via centrifugation and was dried in an oven at 90 °C overnight. The samples are referred to as NMC-0, NMC-0.45, NMC-1.45, and NMC-2.45, in which the numerical value represents the molar ratio of KCl/TM used during calcination.

Differential scanning calorimetry (DSC) and thermogravimetric analysis (TGA) with a Simultaneous Thermal Analyzer STA 449 F3 Jupiter system (NETZSCH, Selb, Bavaria, Germany) were used to study the transformation process of P-NMC to NMC during calcination. Approximately 17 mg of a mixture of P-NMC, LiOH·H₂O, and KCl was prepared, with each ratio of the chemicals corresponding to the ratio required when synthesizing NMC-0, NMC-0.45, NMC-1.45, and NMC-2.45. The mixture was then placed in an alumina crucible and subjected to 25 °C to 850 °C at a heating rate of 10 °C/min, with 1 h hold at 850 °C and a constant airflow of 20 mL/min.

2.2. Characterizations

X-ray diffraction (XRD) measurements were performed for phase analysis with Bruker X-ray Diffraction (XRD) Analysis D8 DISCOVER with a Cu K-alpha source (wavelength $\lambda = 1.54056 \text{ \AA}$ over a range of $2\theta = 5^\circ$ to 120°). The lattice parameters of the crystal structure were obtained through Rietveld refinement over the 10° to 80° range using the HighScore program version 5.2. The morphology of the samples was characterized with a Hitachi Cold FE SU-8000 SEM. Microwave plasma atomic emission spectroscopy (Agilent MP-AES, Santa Clara, CA, USA) was used to confirm the composition ratio of the TM ions of the commercial P-NMC and the synthesized NMC samples. Prior to the MP-AES measurements, the P-NMC and NMC samples were digested using 50 vol.% concentrated hydrochloric acid (<99%, HCl, Sigma-Aldrich), followed by dilution with 2 vol.% nitric acid (TraceMetal Grade, HNO₃, Fisher Scientific, Hampton, NH, USA). A Brunauer-Emmett-Teller (BET) analysis was conducted to measure the specific surface area of the NMC samples using a TriStar 3000 analyzer (Micromeritics, Norcross, GA, USA) in N₂ (-196°C). The particle size distribution was analyzed with Microtrac Flow Sync wet laser diffraction using the dynamic light-scattering analysis mode. Ultrasonication was performed for 60 s before each measurement. X-ray photoelectron spectroscopy (XPS) measurements were conducted using a Thermo-Scientific K-Alpha using an aluminum (Al) K-alpha micro-focused monochromator. The X-ray spot size was set to be 400 μ , and an electron flood gun was used for the charge compensation. The XPS data were analyzed

using Avantage software (Thermo Fisher Scientific, Waltham, MA, USA) for peak fitting of the C 1s, Li 1s, Co 2p, Ni 2p, and Mn 2p spectra with a single peak. The spectrometer energy scale was calibrated using the C 1s peak at 284.8 eV (C–C) as a reference.

2.3. Electrochemical Performance

NMC electrodes were prepared by dispersing the cathode active material with a polyvinylidene fluoride binder (Sigma-Aldrich, $(\text{CH}_2\text{CF}_2)_n$, CAS no.: 24937-79-9) and acetylene black (Alfa Aesar, Ward Hill, MA, USA, average particle size of 60 nm and an area of $75 \text{ m}^2 \text{ g}^{-1}$) in a mass ratio of 9:0.5:0.5 in a N-methyl-2-pyrrolidone solvent. The mixture was homogenized with a Thinky Mixer (Paisley, Toronto, ON, Canada) with 1 mm ZrO_2 grinding balls for 20 min at 300 rpm. The slurry was tape-casted ($\sim 0.005 \text{ g/cm}^2$) using a doctor blade (Bird Applicator Inc., Camano Island, WA, USA, Stainless steel, 006, 9/12) onto Al foil. The electrode was dried at 80°C overnight under a vacuum. The electrode was pressed at 18 tons for 10 s twice after punching out electrode discs with a diameter of 10 mm (0.785 cm^2). A lithium chip (MSE Supplies, Tucson, AZ, USA, diameter 16 mm, thickness 0.6 mm) was used for the anode. Swagelok cells (Stainless steel) were assembled in the order of lithium chip, two polypropylene films (Celgard, Charlotte, NC, USA 2200) of 16 mm as separators, $200 \mu\text{L}$ electrolyte, and cathode disc from bottom to top. The electrolyte was purchased from Sigma-Aldrich and consisted of 1 M of lithium hexafluorophosphate (>97% LiPF_6 , TCI Chemicals, Tokyo, Japan) solution in a 1:1:3 (vol. %) mixture of ethylene carbonate (EC, 99% $(\text{CH}_2\text{O})_2\text{CO}$, Sigma-Aldrich), propylene carbonate (PC, 99.7% $\text{CH}_3\text{C}_2\text{H}_3\text{O}_2\text{CO}$, Sigma-Aldrich), and dimethyl carbonate (DMC, 99% $\text{H}_3\text{COCOOCH}_3$, Sigma-Aldrich) electrolyte plus 2 wt.% tris(trimethylsilyl) phosphite (95% $[(\text{CH}_3)_3\text{SiO}]_3\text{P}$, Sigma-Aldrich) as an additive [29]. The electrolyte composition was selected to withstand high-voltage operation, thereby minimizing parasitic reactions with the cathode [30]. All the cells were assembled under an inert atmosphere in an argon-filled glovebox (MBraun, Garching, Germany). All the cycling data were obtained with an Arbin cycler at room temperature. Electrochemical impedance spectroscopy (EIS) measurements of the NMC samples were taken after 6 h of relaxation time in potentiostatic mode between 0.1 Hz and 100 kHz at open-circuit voltage (OCV).

3. Results and Discussion

3.1. Molten Salt Effect on NMC Crystal Growth

The SEM images of the calcined NMC samples obtained at different KCl/TM molar ratios are presented in Figure 1. By comparing the morphology of the calcined NMC products (Figure 1b–e) to that of the P-NMC (Figures 1a and S2), it is evident that the secondary (aggregated) particles maintained their spheroidal shape.

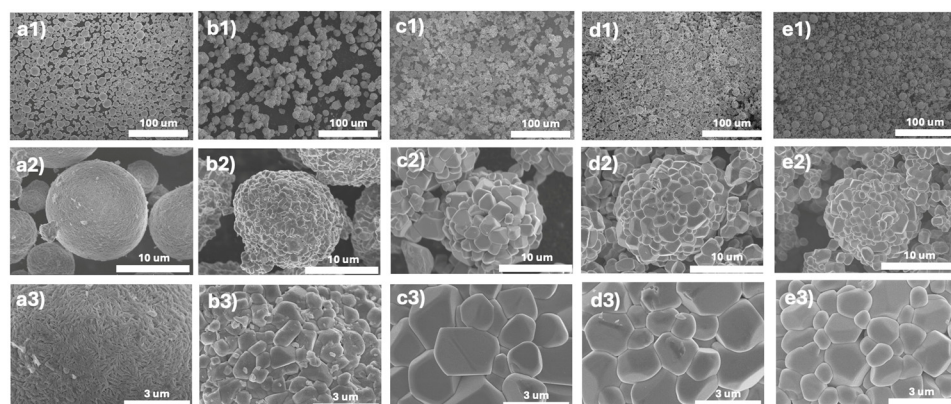


Figure 1. SEM images at different magnifications of NMC commercial hydroxide (P-NMC) (a) and calcined products obtained at different KCl/TM molar ratios: (b) 0, (c) 0.45, (d) 1.45, (e) 2.45. Rows 1, 2, and 3 correspond to progressively higher magnifications for the respective KCl/TM ratios.

NMC-0 (Figure 1b), obtained via conventional solid-state calcination (with no presence of KCl), is seen to have less uniformly shaped primary particles that are smaller than one micron ($0.3 < d_p < 1 \mu\text{m}$). With the presence of molten KCl, an immediate effect on the morphology of the primary particles is observed in that they display distinct crystal facets, assuming an octahedron-like shape. In terms of size, the primary crystallites are observed to be larger for NMCs calcined with molten KCl compared to those of the NMC-0, ranging from $0.8 \mu\text{m} < d_p < 1.8 \mu\text{m}$ for NMC-2.45 and $1.5 \mu\text{m} < d_p < 3 \mu\text{m}$ for NMC-0.45. The growth of primary crystallites is more pronounced for NMC calcined with a lower KCl/TM molar ratio (Figure 1c vs. Figure 1e), suggesting that the primary crystal growth has a dependency on the volume of the molten bath.

Particle size distribution (PSD) resulted in the largest average (secondary) particle size ($40 \mu\text{m}$) for NMC-0 and the smallest for NMC-2.45 ($5.5 \mu\text{m}$), while NMC-0.45 and NMC-1.45 were 6.5 and $18 \mu\text{m}$, respectively. The deviation of the size observed from the SEM is due to the agglomeration of secondary particles, thus a Brunauer–Emmett–Teller (BET) analysis was further conducted to provide a more comprehensive understanding of the particle morphology (Figure 2; and Figure S4 in Supplementary Materials). It is observed that as the KCl/TM molar ratio increases, there is a rather modest change in specific surface area but a significant total pore volume decrease, as shown in Figure 2a,b. This trend suggests that NMC calcined with a lower molten bath volume that exhibits larger individual primary crystals inhibits the formation of tightly packed aggregates, consequently resulting in increased porosity and a slightly higher specific surface area. This is consistent with the SEM images for NMC-0.45 (Figure 1c) that show bulkier primary particles loosely packed compared to the other samples. Surprisingly, the surface area for NMC-0 is comparable to that of NMC-1.45 and NMC-2.45, but with a significantly higher total pore volume. This discrepancy may be due to the BET analysis detecting interparticle voids of the agglomerated NMC-0 secondary particles rather than the internal pores, contributing to a higher pore volume. Nevertheless, the smallest surface area supports the observation of very tightly packed primary particles in NMC-0.

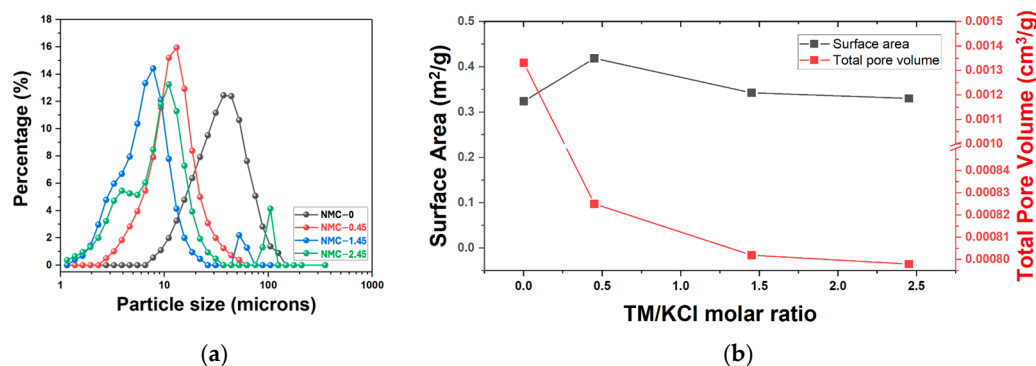


Figure 2. (a) Particle size distribution and (b) specific surface area and total pore volume of the NMC samples obtained with different quantities of molten salt molar ratio of KCl/TM.

3.2. Molten Salt Volume Effect on Crystal Structure

Figure 3a shows the XRD patterns of the NMC calcined products obtained with different KCl/TM ratios. All the diffraction peaks correspond well to a typical layered, hexagonal $\alpha\text{-NaFeO}_2$ structure (space group: $R\bar{3}m$), with no impurity peaks visible.

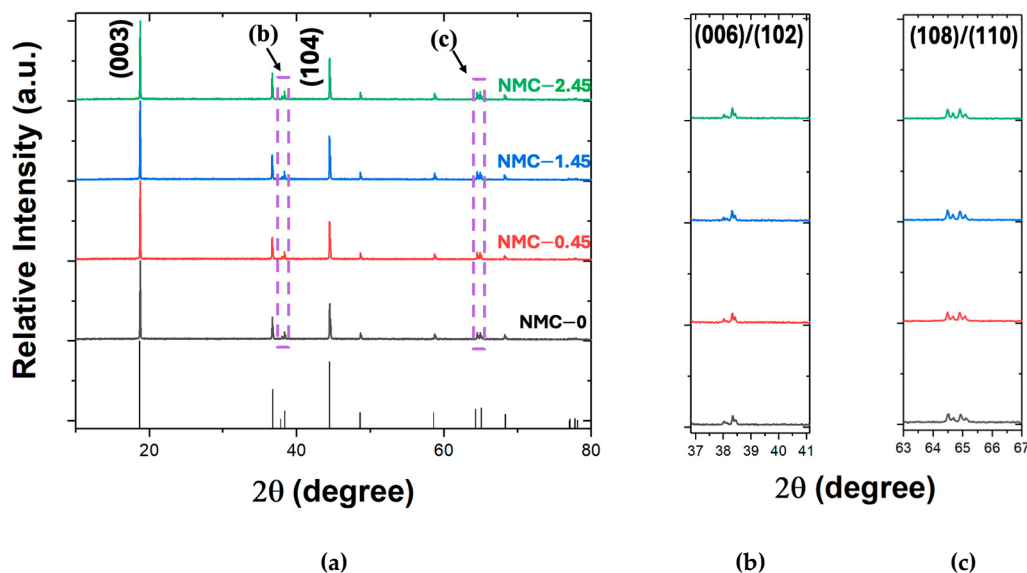


Figure 3. (a) XRD patterns of NMC samples obtained with different KCl/TM molar ratios and enlarged peaks of (b) (006) and (102) and (c) (108) and (110). Reference peaks from JCPDS 00-066-0856 ($\text{LiNi}_{0.8}\text{Mn}_{0.1}\text{Co}_{0.1}\text{O}_2$).

The relative intensity ratio of (003)/(104) peaks ($I_{(003)}/I_{(104)}$) is commonly used as a direct indication of cation mixing, where a higher $I_{(003)}/I_{(104)}$ represents a lower degree of $\text{Li}^+/\text{Ni}^{2+}$ cation mixing, which is a defect caused by Ni^{2+} migration from the transition-metal layer to the lithium layer due to the similar ionic radius of Ni^{2+} (0.69 Å) to that of Li^+ (0.76 Å) [31,32]. As shown in Table 1, all of the NMC samples have $I_{(003)}/I_{(104)}$ values higher than 1.2, representing low cation mixing and well-ordered crystallinity. It is observed that the NMC samples obtained with KCl have $I_{(003)}/I_{(104)}$ slightly lower than the corresponding value of the solid-state calcined NMC-0. Of the three NMC samples obtained in the presence of KCl, NMC-0.45 had the highest $I_{(003)}/I_{(104)}$ ratio (2.0404), implying that a smaller amount of molten salt volume during calcination leads to lower cation mixing. Since the morphological orientation of the crystals may affect the peak intensity [33], XRD refinement has been performed. Contrary to what the relative peak intensity indicates, the percentage of Ni in the Li layer is lower for the NMC samples obtained with KCl present than the solid-state calcined NMC-0, indicating a lower cation mixing for the NMC samples synthesized with KCl. Moreover, there is a trend of slightly increasing cation mixing as the volume of the molten bath increases (1.54 for NMC-0.45 and 1.77 for NMC-2.45), possibly due to the more limited access of oxygen to the particles with the increasing molten bath (Table 1), hindering Ni oxidation from 2+ to 3+, which is crucial for minimizing cation mixing [32,34]. As a consequence, synthesis conditions can significantly affect the degree of cation mixing. For example, lower oxygen partial pressure during calcination leads to less oxidation of Ni^{2+} to Ni^{3+} , resulting in higher cation mixing [35]. At the same time, an increase in calcination temperature leads to a higher degree of cation mixing, especially for Ni-rich NMC, due to the accelerated migration of Ni^{2+} to Li-ion sites. However, high temperatures are necessary for crystal growth to achieve single-crystal NMC. Therefore, maintaining an oxygen-rich atmosphere and using a molten salt bath to promote crystal growth at moderate calcination temperatures are important synthesis parameters to control.

Table 1. XRD relative peak intensity ratio of planes (003) and (104), refined lattice parameters, % of ant-site defects, and weighted profile R-factor (R_{wp}) of the NMC samples. JCPDS 01-088-4075 ($\text{LiNi}_{0.8}\text{Mn}_{0.1}\text{Co}_{0.1}\text{O}_2$) was used as the reference.

Sample	$I_{(003)}/I_{(104)}$	$a, b (\text{\AA})$	$c (\text{\AA})$	% of Ni in Li Layer	R_{wp}^*
NMC-0	2.1468	2.8696	14.1856	1.76	8.05
NMC-0.45	2.0404	2.8707	14.1867	1.54	7.33
NMC-1.45	1.7804	2.8701	14.1835	1.73	6.91
NMC-2.45	1.8702	2.8705	14.1857	1.77	7.13

* The weighted profile R-factor (R_{wp}) is a discrepancy index between the experimental data and fitted model; it is generally accepted that a R_{wp} value lower than 10% indicates a good fit.

Another indicator of the layered crystal structure order is the distinct peak splitting of the (006)/(102) planes (Figure 3b) and (108)/(110) planes (Figure 3c), which is present for all the NMC samples obtained [36].

3.3. Molten Salt Effect on Chemical State

To confirm the oxidation states of Ni, Co, and Mn on the NMC surface, the samples were characterized by XPS (Figure 4).

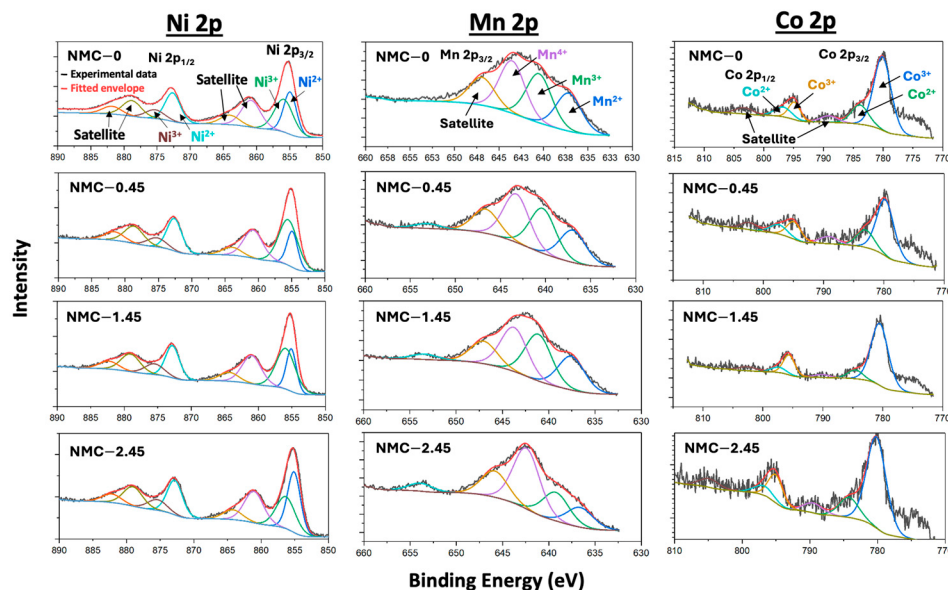


Figure 4. XPS spectra of Ni 2p, Mn 2p, and Co 2p for the NMC samples calcined with different KCl/TM molar ratios.

Starting with the spectra of Ni 2p, the fitting peaks located at 854.9 eV for Ni 2p_{3/2} and 872.6 eV for Ni 2p_{1/2} are ascribed to Ni²⁺, while those at 855.5 eV for Ni 2p_{3/2} and 875.3 eV for Ni 2p_{1/2} are assigned to Ni³⁺ [37]. The Mn 2p spectra have two main peaks of Mn2p_{1/2} and Mn 2p_{3/2}, and peaks located at 637.0 eV, 640.3 eV, and 643.3 eV each indicate Mn²⁺, Mn³⁺, and Mn⁴⁺, respectively [38]. For the Co 2p spectra, the dominant peaks situated at 779.8 eV and 794.9 eV, as per the literature, correspond to Co 2p_{3/2} and Co 2p_{1/2}, respectively, indicating the presence of Co³⁺. The peaks observed at 783.1 eV and 797.5 eV for Co 2p_{3/2} and Co 2p_{1/2}, respectively, suggest the presence of Co²⁺ [37].

Further, we conducted a detailed analysis of Ni on the ratio of 2+/3+ oxidation states in Figure 5. The results of peak fitting for Ni 2p show the Ni²⁺ content to be 37.51% for NMC-0, 30.76% for NMC-0.45, 35.32% for NMC-1.45, and 56.13% for NMC-2.45, showing a trend of decreasing Ni³⁺ content with increasing molten bath volume during calcination. Although the surface oxidation state may not accurately reflect the bulk properties, it indicates that a larger molten bath volume imposes a barrier to the oxidation of TM. This is

also supported by the higher cation mixing for NMC calcined with a larger molten bath volume, as shown in Table 1.

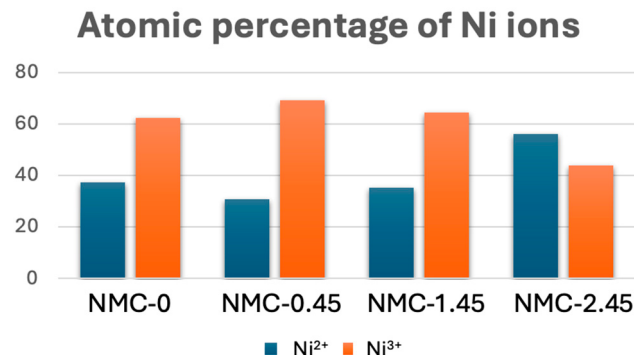


Figure 5. Atomic percentage distribution of Ni²⁺ and Ni³⁺ obtained from XPS analysis of the NMC samples.

3.4. Elemental Composition

An MP-AES analysis was conducted to verify the chemical composition of the NMC samples and to detect any residual KCl impurity, as detailed in Table 2. It has been confirmed that the empirical composition of TM ions of the NMC samples aligns well with that of the P-NMC. Furthermore, there is some negligible potassium impurity in all the samples, including NMC-0, which did not involve KCl in the calcination process. This shows that the presence of K in the sample can be attributed to external contamination and the salt is well removed with the applied sonication-washing step. Note that the NMC-0 sample had not been subjected to such an extra washing step.

Table 2. Elemental composition of different NMC materials.

Sample	Mole % of Ni	Mole % of Mn	Mole % of Co	K/TM
P-NMC	84.10	5.07	11.83	-
NMC-0	83.65	4.81	11.54	0.003
NMC-0.45	83.34	5.06	11.60	0.002
NMC-1.45	83.55	4.72	11.73	0.000
NMC-2.45	83.46	4.91	11.63	0.001

3.5. Molten Salt Effect on Electrochemical Performance

To measure the electrochemical performance of the NMC samples, galvanostatic cycling was conducted at a C/10 rate, with an upper cutoff voltage of 4.2 V to minimize electrolyte oxidation. As shown in Figure 6a, NMC-0.45 resulted in the highest initial capacity of 150.7 mAh/g compared to NMC-0 (124.2 mAh/g), NMC-1.45 (131.5 mAh/g), and NMC-2.45 (120.8 mAh/g). It is important to note that the initial discharge capacity is somewhat lower than the values reported in the literature for NMC811 (~189–200 mAh/g) [39,40]. This discrepancy comes from the relatively lower cut-off voltage of 4.2 V, instead of 4.3 V or 4.5 V, to enhance capacity retention, an essential factor when evaluating the electrochemical performance of the NMC cathode. All the NMC samples calcined with KCl demonstrated stable capacity retention, whereas NMC-0 declined to 92% by the 30th cycle. Interestingly, all the KCl-calcined NMCs exhibited a slight increase in capacity during the initial cycles, resulting in capacity retention over 100%. This may result from slight delithiation during the rinsing process, as these samples underwent an additional sonication step to remove any residual KCl from the pores. All the cells exhibited low Coulombic efficiency (CE) in the first cycle, a common characteristic of Ni-rich NMC cathodes associated with irreversible structural changes during the initial delithiation and the formation of the cathode electrolyte interphase (CEI) [41].

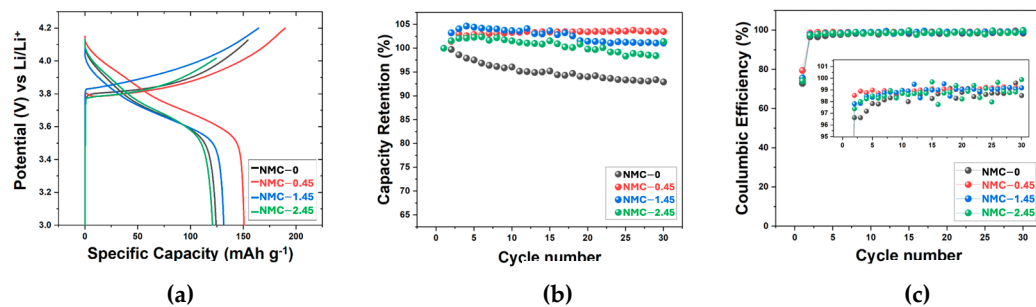


Figure 6. (a) Initial specific discharge capacity vs. voltage profiles, (b) discharge capacity retention, and (c) Coulombic efficiency at C/10 of NMC calcined cathodes obtained with different KCl/TM ratios.

The highest initial discharge capacity of NMC-0.45 may be mainly due to its highest porosity and slightly higher surface area, allowing better electrolyte penetration. Despite NMC-0, NMC-1.45, and NMC-2.45 having comparable surface areas, as reflected in their similar initial discharge capacities, the improved capacity retention of the NMCs calcined with KCl demonstrates the potential of using molten salt during calcination in prolonging the cycle life and improving the stability of the cathode.

3.6. Electrochemical Impedance Spectroscopy (EIS)

To investigate the impact of the molten bath volume during calcination on the electrochemical performance of NMC, we conducted EIS analyses of the pristine state and after the first cycle. Figure 7 provides a direct comparison of the four samples, presenting Nyquist plots alongside their corresponding equivalent circuit model.

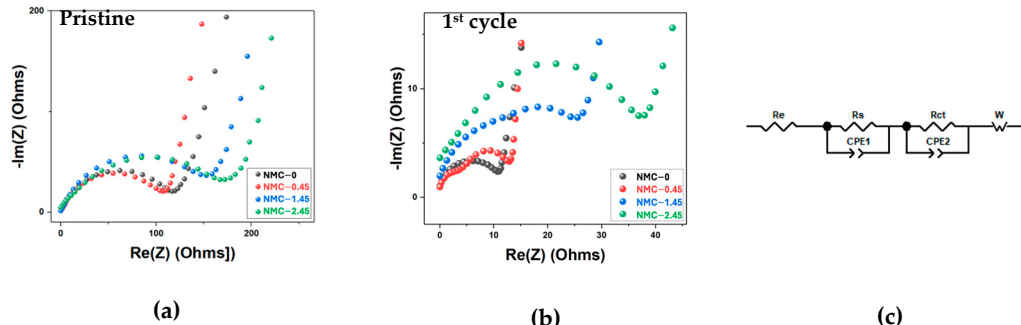


Figure 7. (a) Nyquist plots of NMCs in their pristine state (b) and after the first cycle with (c) the equivalent circuit used to fit the EIS model.

R_e represents the internal resistance of the cell originating from both the material and other components of the battery, **R_s** represents the resistance of the cathode–electrolyte interface layer (CEI), **R_{ct}** represents the charge transfer resistance, and **W** represents the Warburg impedance, which indicates the lithium ions' diffusivity within the electrode. There were two types of EIS data obtained. One featured a single semicircle in the high- and medium-frequency domains, where the diameter corresponds to charge transfer resistance. The other featured a double semicircle in the same frequency domain, where the first corresponds to CEI resistance and the second to charge transfer resistance [42,43]. Though not clearly resolved, the double semicircle is more visible in the NMCs calcined with KCl after their first cycle (observed in NMC-0.45 and NMC-1.45 in Figure 7b), suggesting that the presence of residual KCl introduces an additional resistance, which increases with the amount of KCl used. The absence of double semicircles for NMC-2.45 may be due to the overlapping of the two semicircles to the point where they appear as a single semicircle, as the characteristic frequencies for each process are very close to each other, as seen for NMC-0.45 and NMC-1.45. It is then followed by an inclined line in the low-frequency

region corresponding to Warburg impedance, with a steeper slope indicating slower Li-ion diffusion within the electrode material. In the pristine state, NMC-0.45 exhibited the lowest charge transfer resistance ($107\ \Omega$), significantly less than NMC-1.45 ($153\ \Omega$) and NMC-2.45 ($153\ \Omega$), and comparable to NMC-0 ($117\ \Omega$), despite the potential presence of residual salt that could contribute to the additional resistance. However, after the first cycle, all the samples presented reduced semicircle diameters, a common observation due to enhanced electrolyte penetration, improving the overall electrochemical performance. NMC-0 showed the lowest overall resistance ($11\ \Omega$) post-cycling, followed by the NMC samples calcined with molten salt in the order of increasing molten bath volume. This suggests that even a minute amount of residual molten salt can easily react with the electrolyte to form a CEI, even after a single cycle. Despite the extra resistance from the salt residual, NMC-0.45's overall charge transfer resistance ($13\ \Omega$) remains comparable to that of NMC-0, and this reflects the benefit of using a low volume (KCl/TM molar ratio < 1) of the molten salt bath. The slope of the Warburg impedance in Figure S6 becomes progressively steeper in the order of NMC-2.45, NMC-1.45, and NMC-0.45, indicating an increase in Li-ion diffusion resistance as the molten salt bath volume decreases. This is likely due to the increase in particle size, resulting in a longer diffusion path for the samples calcined with smaller molten salt bath volumes.

Overall, despite the added resistance from residual salts, all the NMC samples calcined with KCl exhibited a higher discharge capacity and improved stability compared to NMC-0, demonstrating the benefits of molten-salt-assisted calcination in the cathode's performance. Among the samples, NMC-0.45 exhibited the best electrochemical performance, achieving significant improvement while maintaining minimal additional resistance from the residual salt. This highlights the importance of optimizing the molten salt bath volume during calcination, as reduced bath volumes allow us to take advantage of molten salt synthesis while minimizing the associated downsides, such as increased resistance from residual salts.

3.7. Crystal Formation Kinetics

We have observed that molten-salt calcination promotes grain growth, resulting in NMC with larger primary particles with distinct facets and smooth surfaces, while solid-state calcination results in aggregated, polycrystalline NMC (Figure 1). To examine the process of crystal growth in molten salt as a function of calcination time, SEM images of NMC-0.45 and NMC-2.45 were taken at $t = 1\text{ h}$, 4 h , 7 h , and 10 h , as shown in Figure 8. Interestingly, despite the same calcination duration, the growth rate of the primary particles varies between NMC-0.45 and NMC-2.45. At $t = 1\text{ h}$, NMC-2.45 shows larger primary particles, indicating a faster initial growth rate than that of NMC-0.45, but after $t = 10\text{ h}$, the final NMC crystal size is larger for the latter. This implies different crystallization pathways between low- and high-volume molten-salt calcination.

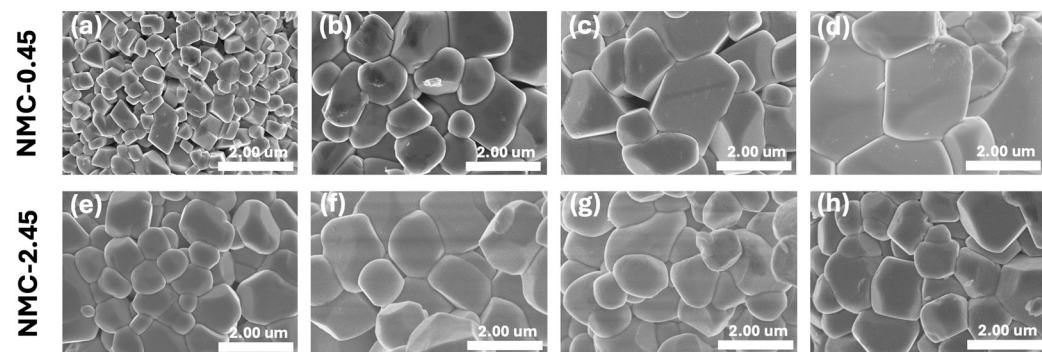


Figure 8. SEM at calcination time stamp of $t = 1\text{ h}$, $t = 4\text{ h}$, $t = 7\text{ h}$, $t = 10\text{ h}$ for NMC-0.45 (a–d) and NMC-2.45 (e–h).

Other physical observations also support the postulation of different crystallization pathways. The BET surface area and total pore volume measurements for NMC-0.45 and

NMC-2.45 at calcination durations of 1 h, 4 h, 7 h, and 10 h (Figure S5) reveal distinct trends in crystal growth behavior. For NMC-0.45, there is a noticeable increase in the total pore volume and surface area between 4 h and 7 h, suggesting that the primary particles became bulkier and led to a looser packing structure. This observation aligns well with the significant crystal growth observed between 4 h and 7 h, as shown in Figure 8b,c. In contrast, NMC-2.45 exhibits a relatively consistent surface area and total pore volume across all the calcination durations, except for the period between 1 h and 4 h. This indicates that most of the crystal growth occurs within the first 1 to 4 h, with minimal changes for the remainder of the duration, as reflected in the SEM images in Figure 8e,h.

To study the change in the crystal structure of the NMC samples calcined with molten salt, XRD profiles for NMC-0.45 and NMC-2.45 at various calcination time stamps were collected, as shown in Figure 9. The clear and sharp peaks indicate that both NMC-0.45 and NMC-2.45 developed a highly crystalline and well-layered crystal structure within the first hour. The relative peak intensity ratio of (003) to (104) slightly decreased over time, suggesting a minor increase in cation mixing as calcination continues, but the change is insignificant. This observation implies that the desired crystal structure is established within the first hour, and the remaining calcination time primarily contributes to crystal growth.

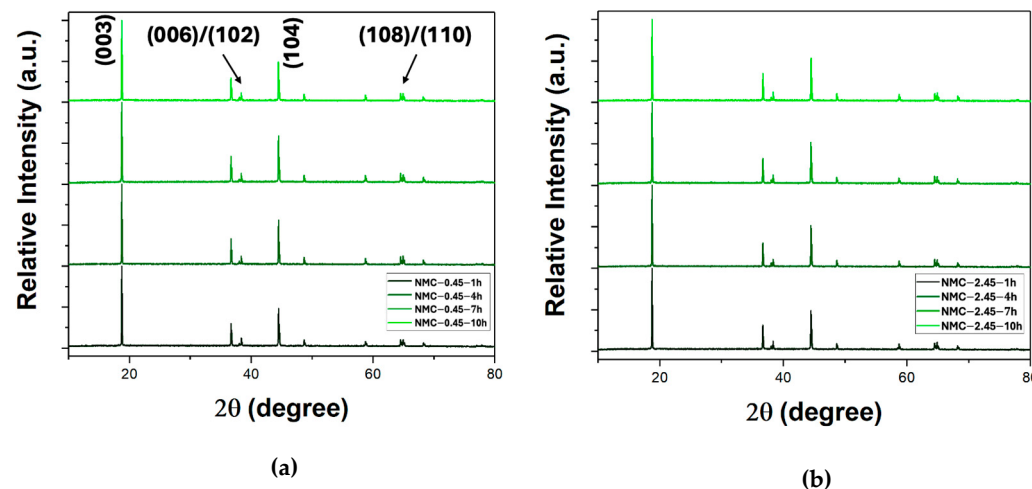


Figure 9. XRD profiles at different time stamps for (a) NMC-0.45 and (b) NMC-2.45.

To gain further insight into the transformation–crystallization process during calcination, differential scanning calorimetry (DSC) measured from 25 °C to 850 °C was performed on the NMC samples, as well as the raw materials KCl, LiOH·H₂O, and P-NMC. The temperature range for the DSC measurements was chosen to replicate the transformation process of our NMC calcination. The holding temperature of 850 °C for our calcination was carefully chosen based on past studies that showed synthesizing well-grown SC-NMC requires a high temperature, but not too high to avoid severe cation mixing [28]. Figure 10a shows the DSC profiles for KCl and the NMC samples over the full temperature range, and Figure 10b shows the profiles in the melting temperature region of KCl. The endothermic peak observed in the NMC samples between 79 °C and 104 °C corresponds to the dehydration of LiOH·H₂O, while the double peaks in the 413 °C to 463 °C range represent the melting of LiOH, aligning well with the endothermic peaks of pure LiOH·H₂O. The endothermic peak between 279 °C and 294 °C corresponds to the decomposition of P-NMC into its oxide form, while the peak between 734 °C and 767 °C indicates the melting of KCl, both of which match the reference peak temperatures. As expected, the endothermic peak area is larger in the NMC samples calcined with higher amounts of KCl.

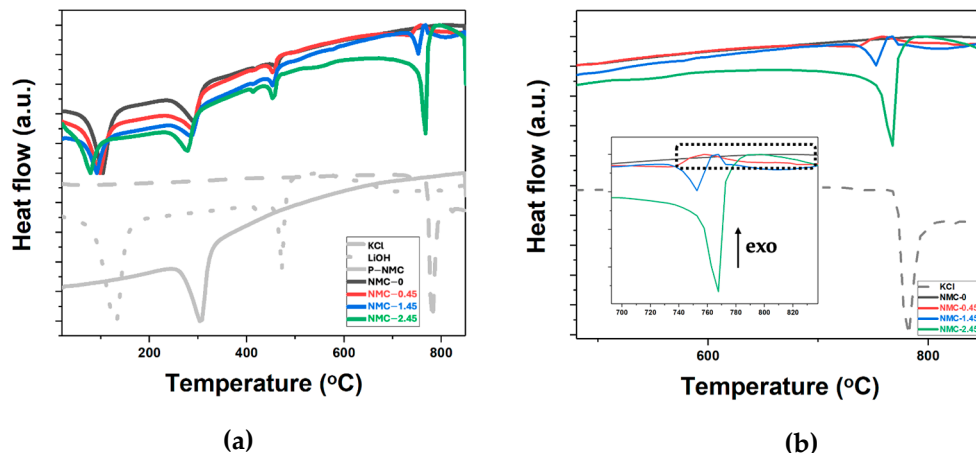


Figure 10. DSC profiles of KCl, LiOH, P-NMC, and NMC samples (NMC-0, NMC-0.45, NMC-1.45, NMC-2.45) measured from 25 °C to 850 °C (**a,b**) and magnified part at high temperature, with the inset highlighting the exothermic peaks.

An interesting observation is that the NMC samples calcined with KCl exhibit an exothermic peak between 750 °C and 800 °C, likely corresponding to the heat released from a structural change to a more stable and ordered layered structure of NMC. This structural change occurred near the melting temperature of KCl, showing the benefits of molten salt in obtaining a more ordered crystal structure. In contrast, NMC-0, calcined without KCl, does not show this exothermic peak. Additionally, no distinct endothermic peak is observed, indicating there is no dissolution of the oxide particles. Meanwhile, the inclined heat flow baseline can represent the continuous (gradual) oxidation/phase transition from the intermediate NMC structure into the layered NMC structure.

3.8. Crystal Growth Mechanism

According to a recent understanding of molten-salt-assisted calcination of NMC, which applies to a high molten bath volume, the process of crystal growth is understood as depicted in Figure 11 [38].

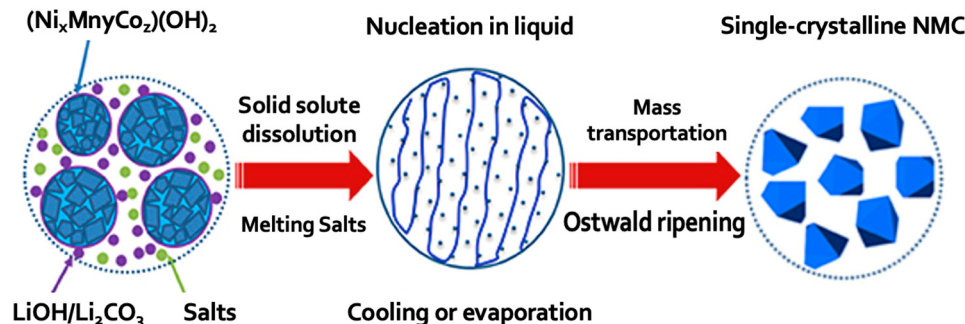


Figure 11. Schematic of growth mechanism of SC-NMC in molten-salt-assisted calcination [38].

Initially, all the precursor particles are fully dissolved in the large molten salt bath, forming a supersaturated constituent metal ion environment, which favors homogeneous nucleation. This generates numerous nuclei, which, depending on the local ion supply, assume different sizes. Following the early formation of nuclei, the phenomenon of Ostwald ripening begins, via which smaller particles dissolve and ion constituents diffuse through the molten salt medium, re-precipitating on larger particles, ultimately growing into dispersed single crystals [38]. In this process, supersaturation is a crucial factor, as it controls crystal growth by directly influencing both the nucleation and growth rates. According to the classical nucleation theory, a larger molten bath, with its lower solute-to-medium ratio, should result in lower supersaturation and thus lead to the growth of larger primary

particles. Interestingly, however, a larger volume of the molten bath during calcination led to the formation of smaller primary particles (Figure 8), which is counterintuitive.

Instead, we propose that the crystal growth mechanism is a hybrid between solid-state transformation and partial dissolution–recrystallization, with the molten salt acting as a mediator rather than an abundant molten salt bath. The P-NMC particles are thought to partially dissolve on the surface level, with the remaining undissolved part serving as both a source for supplying ions into the salt bath via diffusion and as a substrate (seed) that enables heterogeneous nucleation, as depicted in Figure 12.

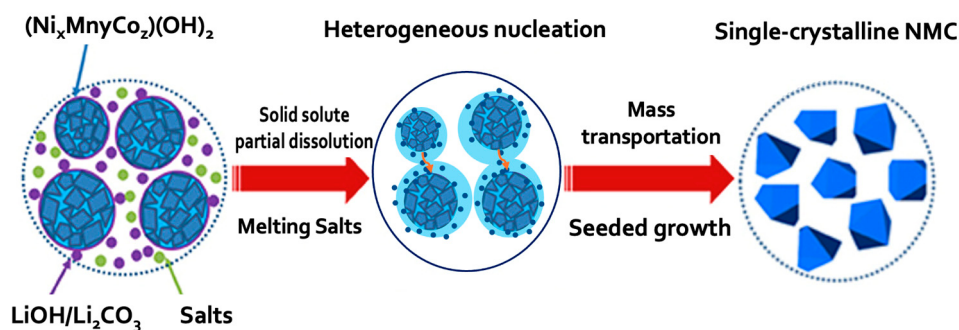


Figure 12. Schematic diagram of the molten-salt-mediated growth mechanism when a low (<1 K/TM) volume of molten salt is used and transformation of the precursor particles to SC-NMC proceeds via partial dissolution and heterogeneous nucleation in enveloping molten salt layers (adapted from [38]).

The molten salt forms an envelope around the P-NMC particles and acts as a mediator where the metal ions are mobilized from the dissolving surface, providing a direct diffusion path for the dissolved species to recrystallize onto nearby heterogeneous nucleation sites. Simultaneously, the core of the particle undergoes a solid-state reaction. Therefore, the smaller the enveloping liquid zone (i.e., less molten bath volume), the shorter the average distance for ion transportation, facilitating fast and efficient transport of ions to the growing crystals. This explains why NMC-0.45 had the largest primary particles among the samples and why the crystal size decreased with the increasing molten bath volume. The distinct rapid initial growth rate for NMC-2.45 is due to the larger molten bath, enabling more efficient dissolution and faster homogeneous nucleation and recrystallization in the early stages of calcination. However, as calcination progresses, the longer ion transport distances combined with the larger number of homogeneously formed nuclei in the larger bath (vis-à-vis the case of fewer heterogeneous nuclei) ultimately led to smaller final single crystals.

These findings demonstrate that a low volume of molten salt (KCl/TM < 1) serves as a mediator promoting large single crystal growth via partial dissolution and heterogeneous recrystallization, ease of washing, and the opportunity to control crystal size by adjusting the volume of the molten salt bath (i.e., ratio of salt to NMC). By carefully managing the molten-salt-mediated calcination process, it is possible to obtain defect-free, well-grown monocrystalline NMC and other cathode materials for optimal electrochemical performance.

4. Conclusions

In summary, this study explores the impact of a reduced molten-salt-to-NMC mass ratio on the crystallization, morphology, and electrochemical performance of Ni-rich single-crystal NMC (SC-NMC) materials via the transformation of precursor NMC hydroxides by oxidative calcination. The results demonstrate that a low molten-salt-to-NMC ratio results in larger primary particles with well-defined facets. A novel hybrid crystallization mechanism was proposed to account for the low molten-salt-mediated calcination process comprising a combination of surface-level partial dissolution–recrystallization and inner core solid-state transformation. Electrochemical performance evaluations revealed that the NMC with the lowest KCl/TM molar ratio of 0.45 exhibited the highest initial discharge capacity and superior capacity retention with no significant impedance compared to the

other samples, confirming the potential of molten-salt-mediated calcination to prolong the cycle life and improve the stability of the cathode. These findings also underscore the advantage of using molten salt as a mediator rather than a large bath. As such, molten-salt-mediated calcination provides a versatile method for optimizing primary (single crystal) and secondary particle morphology, size, and electrochemical performance, thereby contributing to the advancement of high-energy-density, long-cycle Li-ion batteries for electric vehicles and other applications.

Supplementary Materials: The following supporting information can be downloaded at: <https://www.mdpi.com/article/10.3390/batteries10110387/s1>; Table S1: Experimental and theoretical TM composition of the commercial NMC hydroxide precursor (NMC811(OH)_2) obtained with MP-AES.; Figure S1: (a) BET N_2 adsorption/desorption isotherms of the NMC hydroxide precursor with BJH desorption pore size distribution curve in inset. (b) Particle size distribution of the NMC hydroxide precursor; Figure S2: SEM image (left) and XRD profile (right) of the commercial NMC hydroxide precursor ($\text{Ni}_{0.85}\text{Mn}_{0.05}\text{Co}_{0.12}(\text{OH})_2$); Figure S3: XPS Atomic percentage distribution of (a) Co^{3+} and Co^{4+} and (b) Mn^{2+} , Mn^{3+} , and Mn^{4+} obtained from XPS analysis of different calcined NMC products.; Figure S4: BET results: (a) Incremental pore volume and (b) nitrogen adsorption–desorption curve for NMC-0, NMC-0.45, NMC-1.45, and NMC-2.45.; Figure S5: BET surface area and total pore volume measurement for NMC-0.45 and NMC-2.45 as a function of calcination duration $t = 1\text{ h}, 4\text{ h}, 7\text{ h}, 10\text{ h}$; Figure S6: Warburg resistance slope comparison for NMC-0, NMC-0.45, NMC-1.45, and NMC-2.45 obtained from the Nyquist plot. The y-values were adjusted to superimpose the slopes for easier comparison of their differences.

Author Contributions: J.K.K. performed all the experiments and characterizations with the interpretation of the results. G.P.D. supervised all the aspects of this research. The manuscript was written by J.K.K. and revised by G.P.D. All authors have read and agreed to the published version of the manuscript.

Funding: This research was funded by Natural Sciences and Engineering Research Council (NSERC) grant number RGPIN-2022-03978.

Data Availability Statement: The data presented in this study are available in the Supplementary Materials.

Acknowledgments: The authors would like to thank Pierre Hudon for his assistance with the TGA and DSC measurements. OpenAI's ChatGPT (version GPT-4) was used to identify grammatical errors and refine several sentences.

Conflicts of Interest: The authors declare no conflicts of interest.

References

1. Kim, T.; Song, W.; Son, D.-Y.; Ono, L.K.; Qi, Y. Lithium-ion batteries: Outlook on present, future, and hybridized technologies. *J. Mater. Chem. A* **2019**, *7*, 2942–2964. [[CrossRef](#)]
2. Andre, D.; Kim, S.-J.; Lamp, P.; Lux, S.F.; Maglia, F.; Paschos, O.; Stiaszny, B. Future generations of cathode materials: An automotive industry perspective. *J. Mater. Chem. A* **2015**, *3*, 6709–6732. [[CrossRef](#)]
3. Goodenough, J.B.; Kim, Y. Challenges for Rechargeable Li Batteries. *Chem. Mater.* **2009**, *22*, 587–603. [[CrossRef](#)]
4. Orangi, S.; Strømman, A.H. A Techno-Economic Model for Benchmarking the Production Cost of Lithium-Ion Battery Cells. *Batteries* **2022**, *8*, 83. [[CrossRef](#)]
5. Li, W.; Erickson, E.M.; Manthiram, A. High-nickel layered oxide cathodes for lithium-based automotive batteries. *Nat. Energy* **2020**, *5*, 26–34. [[CrossRef](#)]
6. Frith, J. EV Battery Prices Risk Reversing Downward Trend as Metals Surge. Bloomberg.com. 14 September 2024. Available online: <https://www.bloomberg.com/news/newsletters/2021-09-14/ev-battery-prices-risk-reversing-downward-trend-as-metals-surge> (accessed on 14 September 2024).
7. Choi, J.U.; Voronina, N.; Sun, Y.; Myung, S. Recent Progress and Perspective of Advanced High-Energy Co-Less Ni-Rich Cathodes for Li-Ion Batteries: Yesterday, Today, and Tomorrow. *Adv. Energy Mater.* **2020**, *10*, 2002027. [[CrossRef](#)]
8. Saaid, F.I.; Kasim, M.F.; Winie, T.; Elong, K.A.; Azahidi, A.; Basri, N.D.; Yaakob, M.K.; Mastuli, M.S.; Shaffee, S.N.A.; Zolkifly, M.Z.; et al. Ni-rich lithium nickel manganese cobalt oxide cathode materials: A review on the synthesis methods and their electrochemical performances. *Heliyon* **2024**, *10*, e23968. [[CrossRef](#)]
9. Li, T.; Yuan, X.-Z.; Zhang, L.; Song, D.; Shi, K.; Bock, C. Degradation Mechanisms and Mitigation Strategies of Nickel-Rich NMC-Based Lithium-Ion Batteries. *Electrochim. Energy Rev.* **2020**, *3*, 43–80. [[CrossRef](#)]

10. Jiang, M.; Danilov, D.L.; Eichel, R.; Notten, P.H.L. A Review of Degradation Mechanisms and Recent Achievements for Ni-Rich Cathode-Based Li-Ion Batteries. *Adv. Energy Mater.* **2021**, *11*, 2103005. [[CrossRef](#)]
11. Nagda, V.; Ekström, H.; Kulachenko, A. Impact of Mechanical Degradation in Polycrystalline NMC Particle on the Electrochemical Performance of Lithium-Ion Batteries. *J. Electrochem. Soc.* **2024**, *171*, 060526. [[CrossRef](#)]
12. Parks, H.C.W.; Boyce, A.M.; Wade, A.; Heenan, T.M.M.; Tan, C.; Martínez-Pañeda, E.; Shearing, P.R.; Brett, D.J.L.; Jervis, R. Direct observations of electrochemically induced intergranular cracking in polycrystalline NMC811 particles. *J. Mater. Chem. A* **2023**, *11*, 21322–21332. [[CrossRef](#)]
13. Jung, R.; Metzger, M.; Maglia, F.; Stinner, C.; Gasteiger, H.A. Oxygen Release and Its Effect on the Cycling Stability of $\text{LiNi}_x\text{Mn}_y\text{Co}_z\text{O}_2$ (NMC) Cathode Materials for Li-Ion Batteries. *J. Electrochem. Soc.* **2017**, *164*, A1361–A1377. [[CrossRef](#)]
14. de Biasi, L.; Schwarz, B.; Brezesinski, T.; Hartmann, P.; Janek, J.; Ehrenberg, H. Chemical, Structural, and Electronic Aspects of Formation and Degradation Behavior on Different Length Scales of Ni-Rich NCM and Li-Rich HE-NCM Cathode Materials in Li-Ion Batteries. *Adv. Mater.* **2019**, *31*, e1900985. [[CrossRef](#)] [[PubMed](#)]
15. Shishvan, S.; Fleck, N.; McMeeking, R.; Deshpande, V. Cracking and associated volumetric expansion of NMC811 secondary particles. *J. Power Sources* **2023**, *588*, 233745. [[CrossRef](#)]
16. Li, J.; Cameron, A.R.; Li, H.; Glazier, S.; Xiong, D.; Chatzidakis, M.; Allen, J.; Botton, G.A.; Dahn, J.R. Comparison of Single Crystal and Polycrystalline $\text{LiNi}_{0.5}\text{Mn}_{0.3}\text{Co}_{0.2}\text{O}_2$ Positive Electrode Materials for High Voltage Li-Ion Cells. *J. Electrochem. Soc.* **2017**, *164*, A1534–A1544. [[CrossRef](#)]
17. Qian, G.; Zhang, Y.; Li, L.; Zhang, R.; Xu, J.; Cheng, Z.; Xie, S.; Wang, H.; Rao, Q.; He, Y.; et al. Single-crystal nickel-rich layered-oxide battery cathode materials: Synthesis, electrochemistry, and intra-granular fracture. *Energy Storage Mater.* **2020**, *27*, 140–149. [[CrossRef](#)]
18. Li, H.; Li, J.; Ma, X.; Dahn, J.R. Synthesis of Single Crystal $\text{LiNi}_{0.6}\text{Mn}_{0.2}\text{Co}_{0.2}\text{O}_2$ with Enhanced Electrochemical Performance for Lithium Ion Batteries. *J. Electrochem. Soc.* **2018**, *165*, A1038–A1045. [[CrossRef](#)]
19. Song, Y.; Cui, Y.; Li, B.; Geng, L.; Yan, J.; Zhu, D.; Zhou, P.; Zhou, J.; Yan, Z.; Xue, Q.; et al. Revealing the origin of high-thermal-stability of single-crystal Ni-rich cathodes toward higher-safety batteries. *Nano Energy* **2023**, *116*, 108846. [[CrossRef](#)]
20. Qin, Z.; Zhang, T.; Gao, X.; Luo, W.; Han, J.; Lu, B.; Zhou, J.; Chen, G. Self-Reconstruction of Highly Degraded $\text{LiNi}_{0.8}\text{Co}_{0.1}\text{Mn}_{0.1}\text{O}_2$ toward Stable Single-Crystalline Cathode. *Adv. Mater.* **2023**, *36*, e2307091. [[CrossRef](#)]
21. Sangwal, K. *Nucleation and Crystal Growth: Metastability of Solutions and Melts*; John Wiley & Sons: Hoboken, NJ, USA, 2018. [[CrossRef](#)]
22. Kim, Y. Lithium nickel cobalt manganese oxide synthesized using alkali chloride flux: Morphology and performance as a cathode material for lithium-ion batteries. *ACS Appl. Mater. Interfaces* **2012**, *4*, 2329–2333. [[CrossRef](#)]
23. Moiseev, I.A.; Savina, A.A.; Pavlova, A.D.; Abakumova, T.A.; Gorshkov, V.S.; Pazhetnov, E.M.; Abakumov, A.M. Single crystal Ni-rich NMC cathode materials for lithium-ion batteries with ultra-high volumetric energy density. *Energy Adv.* **2022**, *1*, 677–681. [[CrossRef](#)]
24. Spence, S.L.; Xu, Z.; Sainio, S.; Nordlund, D.; Lin, F. Tuning the Morphology and Electronic Properties of Single-Crystal $\text{LiNi}_{0.5}\text{Mn}_{1.5}\text{O}_{4-\delta}$: Exploring the Influence of LiCl-KCl Molten Salt Flux Composition and Synthesis Temperature. *Inorg. Chem.* **2020**, *59*, 10591–10603. [[CrossRef](#)] [[PubMed](#)]
25. Xia, Y.; Chen, A.; Wang, K.; Mao, Q.; Huang, H.; Zhang, J.; He, X.; Gan, Y.; Xiao, Z.; Zhang, W. Industrial modification comparison of Ni-Rich cathode materials towards enhanced surface chemical stability against ambient air for advanced lithium-ion batteries. *Chem. Eng. J.* **2022**, *450*, 138382. [[CrossRef](#)]
26. Qu, Y.; Mo, Y.; Jia, X.; Zhang, L.; Du, B.; Lu, Y.; Li, D.; Chen, Y. Flux growth and enhanced electrochemical properties of $\text{LiNi}_{0.5}\text{Co}_{0.2}\text{Mn}_{0.3}\text{O}_2$ cathode material by excess lithium carbonate for lithium-ion batteries. *J. Alloys Compd.* **2019**, *788*, 810–818. [[CrossRef](#)]
27. Hu, J.; Wang, H.; Xiao, B.; Liu, P.; Huang, T.; Li, Y.; Ren, X.; Zhang, Q.; Liu, J.; Ouyang, X.; et al. Challenges and approaches of single-crystal Ni-rich layered cathodes in lithium batteries. *Natl. Sci. Rev.* **2023**, *10*, nwad252. [[CrossRef](#)]
28. Zhu, J.; Chen, G. Single-crystal based studies for correlating the properties and high-voltage performance of $\text{Li}[\text{Ni}_x\text{Mn}_y\text{Co}_{1-x-y}]\text{O}_2$ cathodes. *J. Mater. Chem. A* **2019**, *7*, 5463–5474. [[CrossRef](#)]
29. Woo, M.; Park, S.-W.; Lee, J.; Seo, D.-H.; Demopoulos, G.P. Attaining full Li-ion storage capacity in defect-free and preferential orientation grown LiCoPO_4 via ab initio solvothermal crystallization control, submitted.
30. Sun, H.-H.; Choi, W.; Lee, J.K.; Oh, I.-H.; Jung, H.-G. Control of electrochemical properties of nickel-rich layered cathode materials for lithium ion batteries by variation of the manganese to cobalt ratio. *J. Power Sources* **2015**, *275*, 877–883. [[CrossRef](#)]
31. Orlova, E.D.; Savina, A.A.; Abakumov, S.A.; Morozov, A.V.; Abakumov, A.M. Comprehensive Study of $\text{Li}^+/\text{Ni}^{2+}$ Disorder in Ni-Rich NMCs Cathodes for Li-Ion Batteries. *Symmetry* **2021**, *13*, 1628. [[CrossRef](#)]
32. Fu, Z.; Hu, J.; Hu, W.; Yang, S.; Luo, Y. Quantitative analysis of $\text{Ni}^{2+}/\text{Ni}^{3+}$ in $\text{Li}[\text{Ni}_x\text{Mn}_y\text{Co}_z]\text{O}_2$ cathode materials: Non-linear least-squares fitting of XPS spectra. *Appl. Surf. Sci.* **2018**, *441*, 1048–1056. [[CrossRef](#)]
33. Inoue, M.; Hirasawa, I. The relationship between crystal morphology and XRD peak intensity on $\text{CaSO}_4 \cdot 2\text{H}_2\text{O}$. *J. Cryst. Growth* **2013**, *380*, 169–175. [[CrossRef](#)]
34. Almazrouei, M.; Park, S.; Houck, M.; De Volder, M.; Hochgreb, S.; Boies, A. Synthesis Pathway of Layered-Oxide Cathode Materials for Lithium-Ion Batteries by Spray Pyrolysis. *ACS Appl. Mater. Interfaces* **2024**, *16*, 33633–33646. [[CrossRef](#)] [[PubMed](#)]

35. Liang, R.; Yu, F.-D.; Goh, K.; Sun, G.; Wang, M.-J.; Zhu, H.; Liu, X.-Y.; Huang, G.-S.; Wang, Z.-B. Influence of oxygen percentage in calcination atmosphere on structure and electrochemical properties of $\text{LiNi}_{0.8}\text{Co}_{0.1}\text{Mn}_{0.1}\text{O}_2$ cathode material for lithium-ion batteries. *Ceram. Int.* **2019**, *45*, 18965–18971. [[CrossRef](#)]
36. Cho, H.; Kim, J.; Kim, M.; An, H.; Min, K.; Park, K. A review of problems and solutions in Ni-rich cathode-based Li-ion batteries from two research aspects: Experimental studies and computational insights. *J. Power Sources* **2024**, *597*, 234132. [[CrossRef](#)]
37. Zhang, M.; Zhao, H.; Tan, M.; Liu, J.; Hu, Y.; Liu, S.; Shu, X.; Li, H.; Ran, Q.; Cai, J.; et al. Yttrium modified Ni-rich $\text{LiNi}_{0.8}\text{Co}_{0.1}\text{Mn}_{0.1}\text{O}_2$ with enhanced electrochemical performance as high energy density cathode material at 4.5 V high voltage. *J. Alloys Compd.* **2019**, *774*, 82–92. [[CrossRef](#)]
38. McNulty, R.C.; Hampson, E.; Cutler, L.N.; Grey, C.P.; Dose, W.M.; Johnson, L.R. Understanding the limits of Li-NMC811 half-cells. *J. Mater. Chem. A* **2023**, *11*, 18302–18312. [[CrossRef](#)]
39. Mao, C.; Ruther, R.E.; Li, J.; Du, Z.; Belharouak, I. Identifying the limiting electrode in lithium ion batteries for extreme fast charging. *Electrochim. Commun.* **2018**, *97*, 37–41. [[CrossRef](#)]
40. Hu, Q.; Wu, Y.; Ren, D.; Liao, J.; Song, Y.; Liang, H.; Wang, A.; He, Y.; Wang, L.; Chen, Z.; et al. Revisiting the initial irreversible capacity loss of $\text{LiNi}_{0.6}\text{Co}_{0.2}\text{Mn}_{0.2}\text{O}_2$ cathode material batteries. *Energy Storage Mater.* **2022**, *50*, 373–379. [[CrossRef](#)]
41. Wang, T.; Ren, K.; He, M.; Dong, W.; Xiao, W.; Pan, H.; Yang, J.; Yang, Y.; Liu, P.; Cao, Z.; et al. Synthesis and Manipulation of Single-Crystalline Lithium Nickel Manganese Cobalt Oxide Cathodes: A Review of Growth Mechanism. *Front. Chem.* **2020**, *8*, 747. [[CrossRef](#)]
42. Li, S.; Li, C.; Yang, T.; Wang, W.; Lu, J.; Fan, W.; Zhao, X.; Zuo, X.; Tie, S.; Nan, J. 3,3-Diethylene Di-Sulfite (DES) as a High-Voltage Electrolyte Additive for 4.5 V $\text{LiNi}_{0.8}\text{Co}_{0.1}\text{Mn}_{0.1}\text{O}_2$ /Graphite Batteries with Enhanced Performances. *ChemElectroChem* **2021**, *8*, 745–754. [[CrossRef](#)]
43. Zhang, Y.; Katayama, Y.; Tatara, R.; Giordano, L.; Yu, Y.; Fraggedakis, D.; Sun, J.G.; Maglia, F.; Jung, R.; Bazant, M.Z.; et al. Revealing electrolyte oxidation via carbonate dehydrogenation on Ni-based oxides in Li-ion batteries by in situ Fourier transform infrared spectroscopy. *Energy Environ. Sci.* **2020**, *13*, 183–199. [[CrossRef](#)]

Disclaimer/Publisher’s Note: The statements, opinions and data contained in all publications are solely those of the individual author(s) and contributor(s) and not of MDPI and/or the editor(s). MDPI and/or the editor(s) disclaim responsibility for any injury to people or property resulting from any ideas, methods, instructions or products referred to in the content.